Structural and magnetic properties of newly found $BaFeO_{2.667}$ synthesized by oxidizing $BaFeO_{2.5}$ obtained via nebulized spray pyrolysis

Stephan Wollstadt [a,d], Yuji Ikeda [b], Abhishek Sarkar [c,e], Sami Vasala [d], Claudia Fasel [f], Lambert Alff [g], Robert Kruk [c], Blazej Grabowski [b], Oliver Clemens [a,*]

[a] University of Stuttgart, Institute for Materials Science, Materials Synthesis Group, Heisenbergstraße 3, 70569 Stuttgart, Germany

[b] University of Stuttgart, Institute for Materials Science, Department of Materials Design, Pfaffenwaldring 55, 70569 Stuttgart, Germany

[c] Karlsruher Institut für Technologie, Institut für Nanotechnologie, Hermann-von-Helmholtz-Platz 1, 76344 Eggenstein Leopoldshafen, Germany

[d] Technical University of Darmstadt, Institut für Materialwissenschaft, Fachgebiet Materialdesign durch Synthese, Alarich-Weiss-Straße 2, 64287 Darmstadt, Germany

[e] Technical University of Darmstadt, Institut für Materialwissenschaft, Gemeinschaftslabor Nanomaterialien, Alarich-Weiss-Straße 2, 64287 Darmstadt, Germany

[f] Technical University of Darmstadt, Institut für Materialwissenschaft, Fachgebiet Disperse Feststoffe, Alarich-Weiss-Straße 2, 64287 Darmstadt, Germany

[g] Technical University of Darmstadt, Institut für Materialwissenschaft, Advanced Thin Film Technology, Alarich-Weiss-Straße 2, 64287 Darmstadt, Germany

* Corresponding Author:

Fax: +49 6151 16 21991
E-Mail: oliver.clemens@imw.uni-stuttgart.de

Abstract

A new vacancy-ordered perovskite-type compound $Ba_3Fe_3O_8$ ($BaFeO_{2.667}$) was prepared by oxidizing $BaFeO_{2.5}$ ($P2_1/c$) with the latter compound obtained by a spray-pyrolysis technique. The structure of $Ba_3Fe_3O_8$ was found to be isotypic to $Ba_3Fe_3O_7F$ ($P2_1/m$) and can be written as $Ba_3Fe^{3+}{}_2Fe^{4+}{}_1O_8$. Mössbauer spectroscopy and *ab initio* calculations were used to confirm mixed iron oxidation states, showing allocation of the tetravalent iron species on the tetrahedral site and octahedral as well as square pyramidal coordination for the trivalent species within a G-type antiferromagnetic ordering. The uptake and release of oxygen was investigated over a broad temperature range from RT to 1100 °C under pure oxygen and ambient atmosphere via a combination of DTA/TG and variable temperature diffraction measurements. The compound exhibits a strong lattice enthalpy driven reduction to monoclinic and cubic $BaFeO_{2.5}$ at elevated temperatures.

1 Introduction

Perovskite oxides offer themselves as candidates for a vast variety of applications, such as cathode materials for solid oxide fuel cells (SOFC) [1-4], membranes [5, 6] and oxygen storage [7]. The oxide perovskite as a crystal type is defined by the general formula ABO_3 where *A* is an alkaline, alkaline earth or rare earth metal cation, and *B* a transition metal cation [8]. Lattice oxygen can also be partially replaced by e.g. halide anions, like F^- [9, 10] or Cl^- [11, 12], even to large extents [13] opening up other fields of applications.

Iron-based perovskite oxides can be reduced and oxidized, resulting in a change of the oxidation state of the transition metal ion from 4+ to 3+. In many cases by reducing the transition metal completely to the trivalent state, the perovskite changes into the defect-ordered brownmillerite structure [14, 15], e.g. $SrFeO_3$ (cubic perovskite) reduced to $SrFeO_{2.5}$ (brownmillerite) [16, 17]. Further, even lower oxidation states are possible that maintain a perovskite related structure by CaH_2-based reduction such as $SrFeO_2$ [18] and $Sr_{1-x}Ba_xFeO_2$ [19] with divalent iron.

Similarly, the perovskite-system Ba-Fe-O possesses a cubic closed-packed (*ccp*) related arrangement of Ba and Fe ions for $BaFeO_{2.5}$, while showing a highly complex vacancy ordered structure of the anions [20-22]. Between an oxygen content of 2.5 and 3, the Ba-Fe-O system exhibits a variety of structures with partial hexagonal closed-packed (*hcp*) stacking of BaO_{3-y} layers [23-25], such as trigonal $BaFeO_{2.64}$ ($R\bar{3}m$) [23] or the hexagonal $P6_3/mmc$ phases $BaFeO_{2.65}$ [26] and $BaFeO_{2.667}$ [25], which can be related to the Goldschmidt tolerance factor [27], which increases for *A* = Ba, and is position-dependent due to the different sizes of Fe^{3+} and Fe^{4+}. The Ba-Fe-O system can adopt a lot of different structures depending of the anion sub-lattice.

$BaFeO_{2.5}$ is susceptible towards topochemical reactions. Several different modifications can be found by introducing OH^-, F^- or more O^{2-}. For example, the fluorine containing cubic ($Pm\bar{3}m$) $BaFeO_2F$ [28] and monoclinic ($P2_1/m$) $Ba_3Fe_3O_7F$ ($BaFeO_{2.333}F_{0.333}$) [29, 30] are formed upon topochemical fluorination of the compound. Hydration of $BaFeO_{2.5}$ yields the orthorhombic (*Cmcm*) phases $BaFeO_{2.33}(OH)_{0.33}$ and $BaFeO_{2.25}(OH)_{0.5}$ [31, 32]. Further, $BaFeO_{2.5}$ can be topochemically oxidized with ozone to $BaFeO_3$ [33]. The oxidation state of the transition metal Fe adapts according to the oxygen content, from 3+ to 4+, which directly affects magnetic properties. $BaFe^{4+}O_3$ is ferromagnetic with a high Curie temperature, however, intrinsic oxygen vacancies change the local oxidation states of iron from 4+ to 3+ [33, 34]. In contrast, $BaFe^{3+}O_{2.5}$ exhibits an antiferromagnetic ordering [20].

We already acknowledged the possible existence of a new monoclinic phase in the oxidic Ba-Fe-O system with an assumed composition of $BaFeO_{2.667}$ in our previous work [35]. There are

several reports mentioning a composition of $BaFeO_{2.667}$, crystallizing either in a hexagonal space group $P6_3/mmc$ [25], or possessing a triclinic structure [23, 36, 37], or adopting a rhombohedral structure [23, 24] for a similar composition $BaFeO_{2.68}$. However, none of these reports were able to derive a precise structural model consistent with the diffraction data observed. In this article, we report a detailed characterization of the synthesis of $BaFeO_{2.667}$ together with its detailed monoclinic structure and magnetic properties, as well as the oxygen incorporation and reduction and the reversibility of this process. An important tool was the in-situ X-ray diffraction which allowed us to monitor the formed phases combined with the knowledge of the already reported isotypic oxyfluorid structure $BaFeO_{2.333}F_{0.333}$. We found that the material shows unusual allocation of Fe^{4+} on a tetrahedrally coordinated site, with antiferromagnetic ordering as well as activity for reversible oxygen uptake and release, an important feature for electrocatalytic applications.

2 Experimental

2.1 Sample synthesis

Synthesis of fine-crystalline precursor material was performed by nebulized spray pyrolysis (NSP), described in more detail previously [38, 39]. The aqueous solution contained the precursor nitrate salts of barium and iron, $Ba(NO_3)_2$ (Sigma Aldrich, 99.99 %) and $Fe(NO_3)_3 \cdot 9\ H_2O$ (Sigma Aldrich, 99.99 %), respectively. The salts were weighed in the stoichiometric ratio 1:1 and dissolved in deionized water. The mixture was stirred for one hour to establish a homogenous transparent yellowish solution. The ultrasonic nebulizer membrane (TDK, NB-59S-09S-0) was operated at a voltage of 48 V and current of 0.5 mA. The formed mist was carried with a constant gas flow of 2.5 SLM (standard liter per minute) of argon through the reactor furnace, which was set to a temperature of 700 °C. A barometer ensured a set pressure of 900 mbar. The powder was collected on a glass-fiber filter, which was held at a constant temperature of 140 °C to prevent water from condensing on the powder. The as-prepared powder was annealed in an air-tight furnace at a temperature of 900 °C under a constant stream of argon for 10 h. The target phase $BaFeO_{2.667}$ was obtained by oxidizing this starting powder at 400 °C in an oxygen atmosphere for 2 h with subsequent quenching to room temperature.

For high temperature impedance spectroscopy, symmetrical films were prepared by spin-coating annealed powder in an acidic dispersion (pH = 4) on YSZ8 button substrates (fuelcellmaterials, Nexceris, USA). The films were then sintered at 1060 °C under argon for 1 h. The film was

oxidized at 400 °C in an oxygen atmosphere for 2 h with subsequent quenching to room temperature. Subsequently, both sides were coated with a sputtered Au electrode.

2.2 X-ray Diffraction Experiments

Ambient and high temperature X-ray diffraction (XRD) experiments were carried out on a Bruker D8 diffractometer (Bruker AXS, Karlsruhe, Germany) with Bragg-Brentano geometry and a Cu-Kα source. For ambient measurements the angular range was set to 20° to 100° 2θ with a step size of 0.02° and 1 second measurement time per step. The high temperature diffraction experiments were carried out in an HTK 1200 N temperature chamber with a TCU 1000 N (Anton Paar) temperature controller. The oxidation behavior of $BaFeO_{2.5}$ was investigated under a pure oxygen atmosphere, while the stability of $BaFeO_{2.667}$ was investigated under air. In order to obtain a satisfying quality of the patterns, the angular range was reduced to 20° to 60° 2θ with a step size of 0.008° and 0.22 seconds per step. A constant oxygen flow ensured a homogenous oxygen atmosphere. The temperature range was set from room temperature to 1080 °C. Each obtained pattern was qualitatively and quantitatively evaluated and refined using the Rietveld method implemented in the software TOPAS 6 (Bruker AXS, Karlsruhe, Germany). Therefore, the instrumental contribution to the convolution function was extracted empirically from a set of fundamental parameters utilizing a reference scan of a LaB_6 standard (NIST 660a).

2.3 TG/DTA

Thermogravimetric analysis and differential thermal analysis were carried out on a Netzsch STA 449C. The temperature range was set from room temperature to 1100 °C (5 °C/min) under flowing oxygen (40 ml/min).

2.4 Magnetic measurements

Magnetization measurements were done using a Quantum Design MPMS SQUID magnetometer. The sample powder was filled into a gelatin capsule and fixed into a plastic sample holding straw. Temperature dependent $M(T)$ behavior was measured in zero-field-cooled (ZFC) and field-cooled (FC) modes between 10 K and 350 K at 1 T field. Also, field dependent M(H) measurements were done at 10, 80, 250 and 320 K between −5 T and 5 T with 0.1 T intervals.

2.5 ^{57}Fe Mössbauer spectroscopy

^{57}Fe Mössbauer spectroscopy measurements were performed in transmission geometry using a spectrometer with a moving source of ^{57}Co:Rh in transmission geometry using a triangular sweep of the velocity scale. Low temperature measurements were performed using a liquid He

flow cryostat. As conventionally done, the isomer shift is given relative to α-Fe at room temperature.

2.6 DFT calculations

In the present *ab initio* calculations for $BaFeO_{2.667}$ we considered the G-type antiferromagnetic (AFM) ordering as well as the ferromagnetic (FM) and the non−magnetic (NM) ordering. To achieve a commensurate sampling of all the magnetic configurations, a 56-atom supercell based on a 1×1×2 expansion of the 28-atom primitive cell was employed in the present *ab initio* calculations.

The projector augmented wave method [40] and the generalized gradient approximation (GGA) of the Perdew−Burke−Ernzerhof (PBE) form [40] as implemented in the VASP code [41, 42] were applied in combination with the provided potentials [43]. The 5*s*5*p*6*s*, 3*d*4*s* and 2*s*2*p* orbitals of Ba, Fe and O, respectively, were treated as valence states. The plane-wave cutoff was set to 550 eV. The reciprocal space of the 56-atom supercell was sampled by a Γ-centered 6 × 8 × 4 mesh, and the Methfessel−Paxton scheme [44] with a smearing width of 0.1 eV was employed. Total energies were minimized until they were converged to within 10^{-5} eV per unit cell. Cell volume, cell shape, and internal atomic positions were optimized so that the forces on atoms and the stress components on the supercells are less than $2.5 \cdot 10^{-2}$ eV/Å and $1 \cdot 10^{-3}$ eV/Å^3, respectively. The NM, FM, and G-AFM configurations were computed under the collinear spin-polarized condition. Strong on-site electron correlation was considered for the Fe *d* orbitals employing the rotationally invariant DFT+*U* formalism of Dudarev *et al.* [45], with $U_{\text{eff}} \equiv U - J$ varied in a range of 0 eV to 6 eV. Volumes, charges, and magnetic moments of atoms were evaluated based on the Bader analysis [46] employing the Yu−Trinkle algorithm [47] as implemented by Henkelman *et al.* [48-50].

For comparison, similar calculations were performed on cubic $Pm\bar{3}m$ $BaFeO_3$. Previous *ab initio* simulations found that, within the collinear spin polarization, the FM phase is thermodynamically more stable than the AFM phases at 0 K for $BaFeO_3$ [51-53], and we therefore focus on the FM phase for $BaFeO_3$. The reciprocal space of the 5-atom cubic primitive unit cell was sampled by a Γ-centered 12 × 12 × 12 mesh, and otherwise the same computational conditions as for $Ba_3Fe_3O_8$ were applied.

3 Results and discussion

3.1 Determination of optimized synthesis conditions for $BaFeO_{2.667}$

The diffraction experiments on the oxidation behavior under a pure oxygen atmosphere of monoclinic $BaFeO_{2.5}$ prepared by NSP are presented in Figure 1 a,c,e. All compositions given are in good agreement with the weight changes observed in a DTA/TG measurement (see Figure 2 and an extensive discussion in SI). The compound starts to take up oxygen around 250 °C under the formation of a new phase $BaFeO_{2.667}$ with monoclinic ($P2_1/m$) symmetry (see structural analysis discussed in section 3.2), with a diffraction pattern not reported before. During this oxidation, the unit cell shrinks due to the change in the valence of iron from the bigger trivalent to the smaller tetravalent state [54, 55]. Oxygen is again released starting at 475 °C under the reformation of $BaFeO_{2.5}$ ($P2_1/c$), where both phases coexist up to a temperature of ~ 580 °C. Around 750 °C the system changes into a mixture predominantly consisting out of the hexagonal $P6_3/mmc$ ($BaFeO_{2.667}$) [25] and a lower amount of a cubic phase ($Pm\bar{3}m$), and the latter becomes the main phase at a temperature of 1000 °C.

The transformation to the oxygen richer phases with $P2_1/m$ or $P6_3/mmc$ symmetry is accompanied by a decrease of the pseudocubic lattice parameter $a_{pseudocubic}$, which is calculated from the cube root of the volume per $BaFeO_{2.5+x}$ formula unit, $V_{f.u.}$. In contrast, the transformation of $BaFeO_{2.5}$ $P2_1/c$ above 750 °C appears to turn into $Pm\bar{3}m$ due to a sufficient amount of thermal energy (see Figure 2). The changes in volume and the linear expansions from the different pseudocubic lattice parameters are highlighted in Figure 1 e.

The narrow stability range of the monoclinic phase $P2_1/m$ ($BaFeO_{2.667}$) becomes also evident by heating the as-prepared $BaFeO_{2.667}$ sample in air, i.e., reducing the oxygen partial pressure from 1 bar to 0.2 bar (see Figure 1 b,d,f). In air, $BaFeO_{2.667}$ starts to release oxygen at around 300 °C, forming the monoclinic $BaFeO_{2.5}$ phase ($P2_1/c$). It remains in this configuration until it eventually starts to transform to cubic $Pm\bar{3}m$ symmetry at around 800 °C, as already observed under oxygen atmosphere. This structural transition only reflects the breaking up of the long range oxygen vacancy order found for $BaFeO_{2.5}$ ($P2_1/c$) [20]. During this transition, no other oxidized phase is formed as in case of BFO under oxygen, compare Figure 1 c and d, respectively. The maintenance of oxygen composition for the $P2_1/c$ to $Pm\bar{3}m$ is also indicated from the absence of a sudden change of the volume per formula unit, see Figure 1 e,f. Further, we found that cooling $BaFeO_{2.667}$ slowly under oxygen results in an oxygen uptake under formation of tetragonal $BaFeO_{2.81}$ between 200-300 °C, which can also be found as an impurity phase (see next section) depending on the detailed heating and cooling conditions chosen. Thus, the uptake of

oxygen under transformation to $BaFeO_{2.81}$ is a competing reaction when heating $BaFeO_{2.667}$ in pure oxygen atmosphere, and is similar to the oxygen uptake of $BaFeO_{2.5}$ under formation of cubic $BaFeO_3$ at 150 °C when heating under ozone as reported by Hayashi et al. [33].

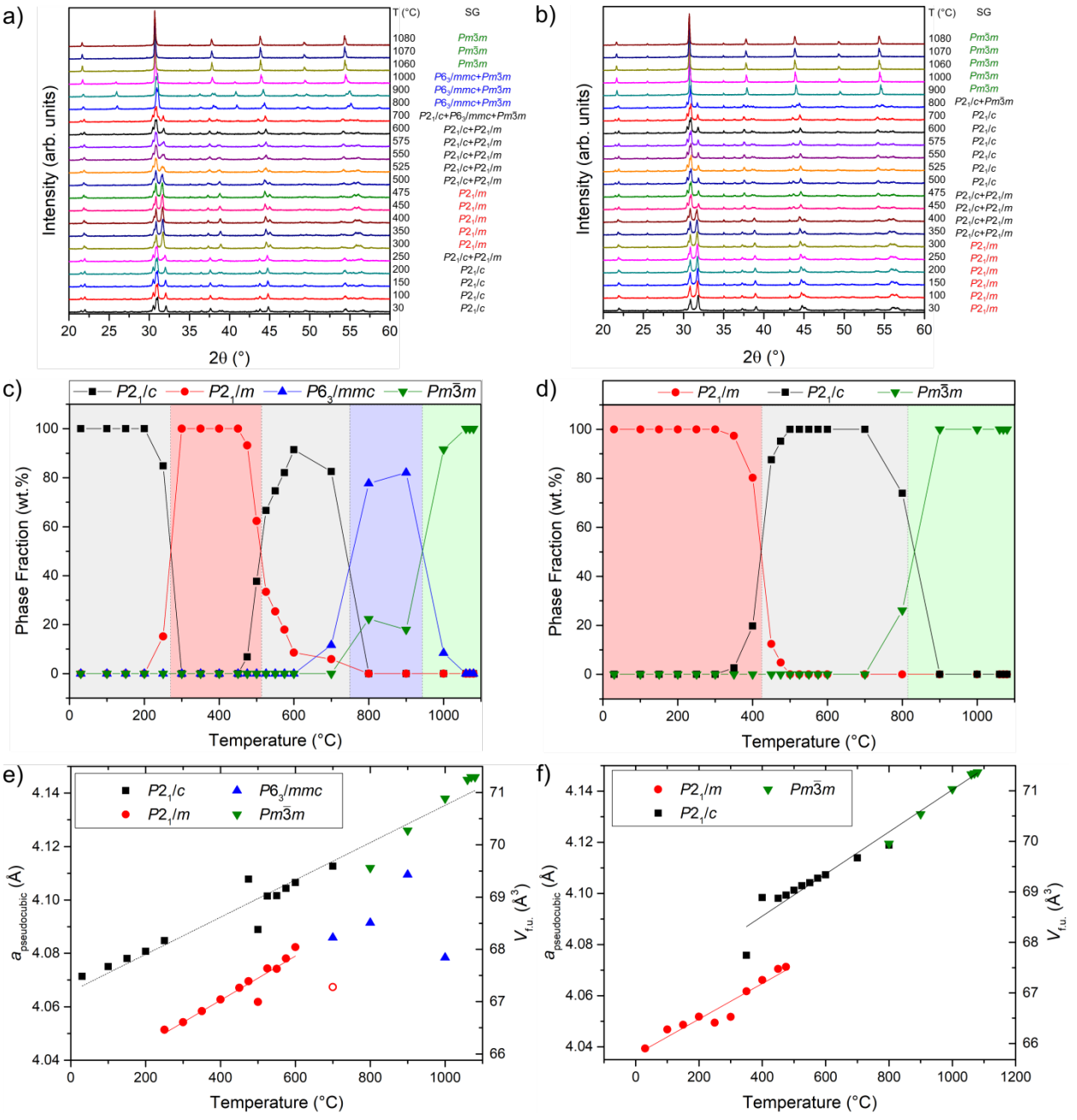

Figure 1: Results of the high temperature XRD study: (a,c,e) depict the results of $BaFeO_{2.5}$ under oxygen; (b,d,f) depict the results of $BaFeO_{2.667}$ under air. (a,b) show the XRD pattern over the whole temperature range with the emerging configurations. (c,d) highlight the corresponding phase fractions as calculated by Rietveld refinements. (e,f) showcase the evolving pseudo-cubic lattice parameters (and simultaneously the volume per formula unit $V_{f.u.}$).

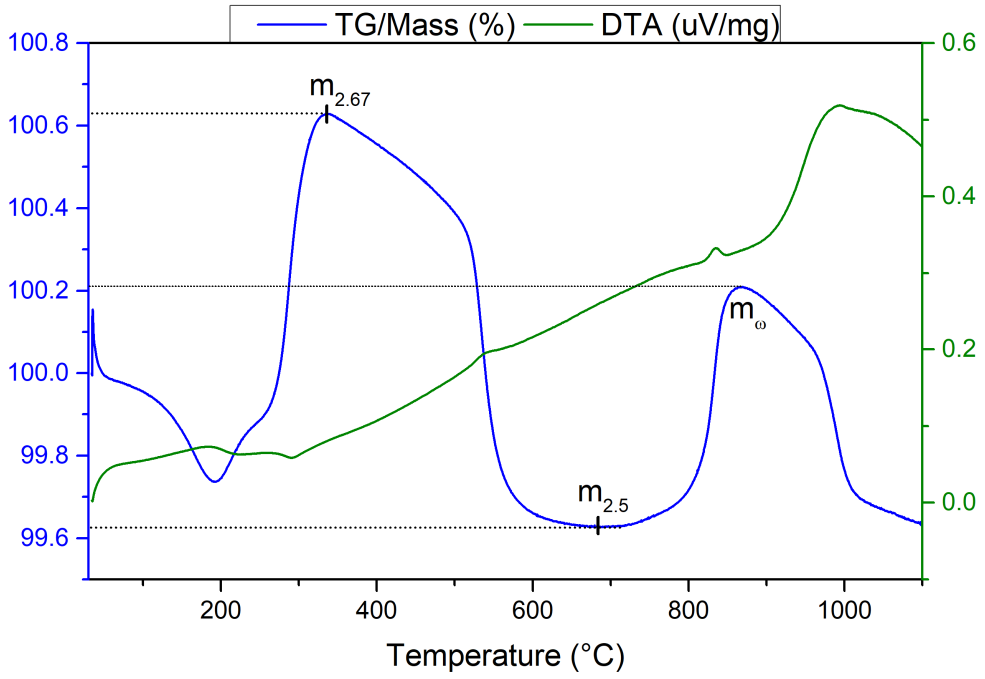

Figure 2: TG/DTA measurement of pure $BaFeO_{2.5}$ performed under pure oxygen atmosphere, complementary to the HTXRD experiment depicted in Figure 1 a,c,e.

3.2 Structural characterization of $BaFeO_{2.667}$

After obtaining optimized synthesis conditions, a long-time scan of $BaFeO_{2.667}$ was recorded at ambient temperature. Indexing of this pattern indicated the compound to crystallize in the monoclinic crystal system, with lattice parameters indicating a $\sqrt{6}$ x $\sqrt{2}$ x $\sqrt{3}$ supercell of the cubic perovskite type structure, i.e., a 6-fold superstructure of the cubic perovskite. To the best of our knowledge, this symmetry is known only for $BaFeO_{2.333}F_{0.333}$ [29, 30] as well as for $BaCoO_{2.667}$[56], i.e., 2 $Ba_3M_3X_8$ = $Ba_6M_6X_{16}$ for using integer chemical indexes, and both compounds have been found before by members of our group. Indeed, the pattern could be well fitted based on the structure found for $BaFeO_{2.333}F_{0.333}$ [29, 30]. In comparison to $BaFeO_{2.333}F_{0.333}$ ($V_{oxyfluoride,\ f.u.}$ = 67.10 Å³ [30]), $BaFeO_{2.667}$ ($V_{oxide,\ f.u.}$ = 66.47(2) Å³) exhibits a significantly smaller unit cell volume, which can be related to the smaller atomic radius of Fe^{4+} as compared to the single valence of the larger Fe^{3+} found in the oxyfluoride compound. The characteristic XRD reflexes in the range of 29 to 33° are shown in Figure 4 a) to showcase the differences between the parent oxide $BaFeO_{2.5}$ and the oxidized $BaFeO_{2.667}$ and oxyfluoride $BaFeO_{2.333}F_{0.333}$. Since the monoclinic structure of $BaFeO_{2.5}$ is not directly related to the monoclinic structure of $BaFeO_{2.667}$ via a group-subgroup relationship (see symmetry trees given in [20, 29, 57]), it is not possible to refine the reflection splitting pattern observed for $BaFeO_{2.667}$ by adjusting the lattice parameters within the

$P2_1/c$ structural model. Thus, it is possible to rule out such, at first glance likely, compositionally similar ordering variants.

We acknowledge that in addition to the monoclinic phase, another perovskite-phase was observed in the powder quenched to room-temperature ($P4/mmm$, a = 3.981 Å, c = 4.010 Å, V = 63.53 Å³) with a weight fraction of around 10 %. This tetragonal structure is formed during the cooling process after oxidation and cannot be completely avoided by quenching to room temperature. Such a tetragonal barium ferrate was reported previously [23], and assigned to a composition of $BaFeO_{2.81}$ (a = 3.978 Å, c = 4.003 Å); thus it shows that the further uptake of oxygen on cooling cannot be avoided completely.

Due to the fact that we could not get neutron data for the compound, which makes a precise determination of oxygen positions impossible, the atomic positions were derived by relaxing the structural model within the DFT calculations. Figure 3 shows the unit cell of the oxygen-vacancy-ordered $BaFeO_{2.667}$ ($Ba_3Fe_3O_8$) structure, based on O for F substitution of the structural model of $BaFeO_{2.333}F_{0.333}$. The structural parameters are listed in Table 1 and Table 2 (with U_{eff} = 2.5 eV, which is close to the value used in [58] ($U - J$ = 2.4 eV) and reproduces a helical spin order in $BaFeO_3$ as observed in experiments). The structure obeys the symmetries of the space group $P2_1/m$ with Z = 6. Apart from changes of bond distances, as well as smaller changes of bond angles, no significant change was observed regarding the principle coordination environments. In particular, there are three symmetrically inequivalent sites for Fe, which are coordinated by O atoms in octahedral, pyramidal, and tetrahedral arrangements, respectively. Thus, the coordination scheme and connectivity of iron coordination polyhedra within $BaFeO_{2.667}$ can be described by the formula $Ba_3(FeO_{6/2})(FeO_{5/2})(FeO_{3/2}O_{1/1})$.

Both, the positional parameters of $BaFeO_{2.333}F_{0.333}$ as well as the DFT-optimized parameters for $BaFeO_{2.667}$ can be used to give a sufficiently good fit of the recorded diffraction patterns, as shown in Table 2 and Figure 4 b,c.

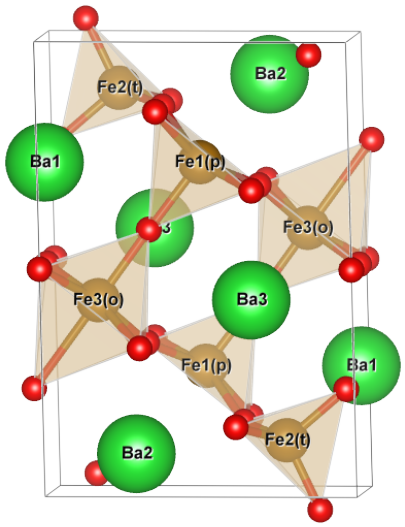

Figure 3. Primitive cell of $Ba_3Fe_3O_8$ (BaFeO2.667). Green, brown and red spheres represent Ba, Fe, and O atoms, respectively. The labels on the Fe atoms show their coordination environments; "o", "t" and "p" indicate an octahedral, tetrahedral, and pyramidal coordination, respectively.

Table 1: DFT optimized internal atomic positions of G-AFM $P2_1/m$ $Ba_3Fe_3O_8$ with U_{eff} = 2.5 eV. For Fe atoms, the coordination environments are indicated.

Element	Wyckoff	Coordination	*x*	*y*	*z*
Ba	2*e*		0.271	1/4	0.987
	2*e*		0.911	1/4	0.716
	2*e*		0.573	1/4	0.336
Fe	2*e*	Fe1 pyramidal	0.270	1/4	0.489
	2*e*	Fe2 tetrahedral	0.881	1/4	0.233
	2*e*	Fe3 octahedral	0.574	1/4	0.827
O	2*b*		½	0	0
	2*e*		0.768	1/4	0.038
	2*e*		0.418	1/4	0.658
	2*e*		0.033	1/4	0.132
	4*f*		0.674	0.999	0.685
	4*f*		0.846	0.991	0.383

Table 2: Lattice parameters optimized in DFT calculations and with XRD measurements. For XRD, the parameters were obtained with fixing the atomic positions either to those of isotypic $BaFeO_{2.333}F_{0.333}$ [30] or those of our DFT results. Fits are shown in Figure 4.

	DFT	XRD (atomic positions fixed)	
		$BaFeO_{2.333}F_{0.333}$ (isotypic to $BaFeO_{2.667}$)	based on DFT input
a [Å]	10.290	10.1597(2)	10.1621(2)
b [Å]	5.687	5.65021(15)	5.64942(14)
c [Å]	7.074	6.9524(2)	6.95256(19)
β [°]	91.457	92.0529(17)	92.0490(19)
$V_{f.u.}$ [Å³]	68.97	66.47(2)	66.48(2)
R_{wp} (%)		2.81	3.12
GOF		1.55	1.72

Both, the coordination scheme as well as the presence of Fe^{4+} can be well confirmed by Mössbauer spectroscopy (see Figure 5 and Table 3, sextet 3). The Mössbauer spectrum of the compound was recorded at 10 K, at which the spectrum was easier to interpret than at ambient temperature (see Figure S 1). At 10 K, the spectrum could be well described by three sextets with areas in the ratio of ~ 1:1:1 (Table 3), agreeing well with iron being located on three different crystallographic sites with local symmetry 2*e.* One of these sextets showed an isomer shift of 0.08 mm/s and a hyperfine field of 27.5(1) T, and we assign this sextet to the tetravalent iron species due to the following reasons: The reduction of the hyperfine field is well explained from the lower number of unpaired spins found for Fe^{4+} (d^4) as compared to Fe^{3+} (d^5). The fact that the isomer shift is larger to what has been found for Fe^{4+} in Na_4FeO_4 (-0.140 mm/s [59]), Ba_2FeO_4 and Ba_3FeO_5 (-0.152 mm/s and -0.142 mm/s, respectively [60]), can be explained from the different bonding scenarios of the compounds. These compounds have isolated FeO_4^{4-} tetrahedra, which do not share edges or corners with other FeO_4^{4-} tetrahedra. Therefore, the oxygen ions provide a stronger degree of covalent bonding to the iron in compounds with non-linked FeO_4^{4-} tetrahedra, which reduces the isomer shift of the iron species in Na_4FeO_4, Ba_2FeO_4 and Ba_3FeO_5.

The other two sextets both possess significantly higher isomer shifts and hyperfine fields of 0.31 mm/s and 0.55 mm/s and 50.4(1) T and 47.0(1) T, respectively. Both, hyperfine field and isomer shifts are well indicative for trivalent iron, similar to the what has been found for $BaFeO_{2.5}$ [20] and $BaFeO_{2.333}F_{0.333}$ [29]. Thus, one can conclude that charge ordering occurs in $BaFeO_{2.667}$ due to the significantly different site potentials induced by the different coordination environments.

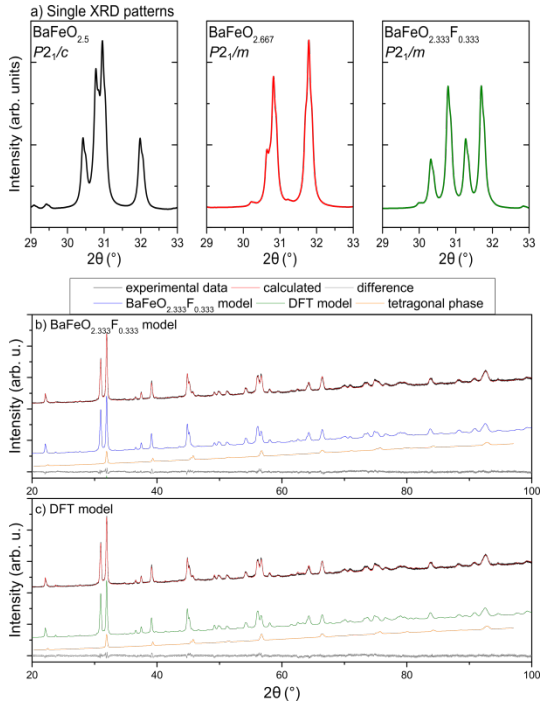

Figure 4. a) Characteristic XRD reflexes for $BaFeO_{2.5}$, $BaFeO_{2.667}$ and $BaFeO_{2.333}F_{0.333}$. Ambient XRD data of $BaFeO_{2.667}$ and corresponding Rietveld fit based on the positional parameters found for b) $BaFeO_{2.333}F_{0.333}$ [29] and c) calculated by DFT for $BaFeO_{2.667}$.

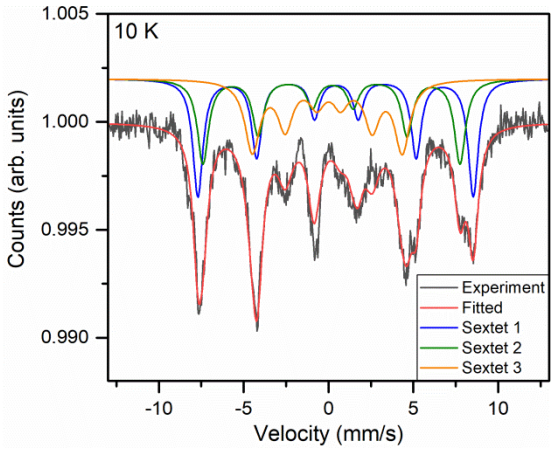

Figure 5. ^{57}Fe Mössbauer spectra at 10 K of $BaFeO_{2.667}$.

Table 3. Fitting parameters for the ^{57}Fe Mössbauer spectrum of $BaFeO_{2.667}$ recorded at 10 K.

	Sextet 1 (blue)	**Sextet 2 (green)**	**Sextet 3 (orange)**
Area (%)	37(2)	29.5(1)	33.5(2)
Isomer shift (IS) (mm/s)	0.55(1)	0.31(1)	0.08(2)
Hyperfine field Bhf (T)	50.4(1)	47.0(1)	27.5(1)
Quadrupole splitting (mm/s)	-0.05(2)	-0.07(3)	-0.08(3)

Thus, we discuss the allocation of the tetravalent iron species on one of the three different sites in the following. To do so, it is important to review what has been found for similar compounds previously. First, for an octahedrally coordinated tetravalent iron ($Fe^{4+}O_{6/2}$), no strong tendency was found for distortion of the octahedron, though this would be in principle expected from the electron configuration $t_{2g}^3e_g^1$ of high spin Fe^{4+} [61-65]. The high spin Fe^{4+} can be stabilized inside the square pyramidal coordination ($Fe^{4+}O_{5/2}$) as it has been observed for $SrFeO_{3-\delta}$ [66] next to octahedral coordination of the trivalent species ($Fe^{3+}O_{6/2}$) or inside $BaY_{0.5}Fe_{0.5}O_{2.75}$, where a square pyramidal coordination of Fe^{4+} is favored, while $BaY_{0.5}Fe_{0.5}O_{2.5}$ exhibits only octahedrally and tetrahedrally coordinated Fe^{3+} [65]. For $Sr_{1-x}Ba_xFeO_2$ ($0.4 \leq x \leq 1$) it was found that high spin Fe^{2+} (S = 2) is 4-fold coordinated inside a square-planar configuration [19]. By oxidizing $CaAl_{0.5}Fe_{0.5}O_{2.5+\delta}$, the tetrahedrally coordinated Fe^{3+} turns into Fe^{4+}, 5-fold coordinated inside a square pyramid [67]. Apart from perovskite type compounds, 4-fold coordinated high-spin Fe^{4+} was found within the compound Na_4FeO_4 [59], but it is also present within other non-perovskite-type compounds of the Ba-Fe-O system, namely in the Ba-rich Ba_2FeO_4 and Ba_3FeO_5 [60]. These structures are composed of isolated FeO_4^{4-} tetrahedra, as it was also reported for other Ba_2MO_4 compounds, with M being Ti, V, Cr or Co [68-74], with only small distortion of the tetrahedra due to Jahn-Teller active electron configuration. Inside the tetrahedron, Fe^{4+} adapts the electronic configuration $t_{2g}^2e_g^2$, with a total spin of S = 2, e.g. high spin, which is the only observed spin state observed in solid state materials [75]. On the other side, for similar compounds with smaller *A*-site cations, e.g. Sr_2FeO_4 [70], the Fe^{4+} cation coordination is an almost perfect octahedron, though the site symmetry of 4/*mmm* would allow for significant stretching of the octahedron. As a simple conclusion, the increase of coordination number for barium seems to induce the lowering of the coordination number for the tetravalent iron species within polyhedra of reduced coordination number.

To derive the most plausible allocation of the tetravalent iron atoms, bond valence sums (BVS) [76] were calculated based on Fe-O distances derived from the structure optimized by the *ab initio* calculations. These calculations clearly indicate that Fe^{4+} is located on the tetrahedrally coordinated site (Fe2, see Table 4). This is in principle agreement with what we found for isotypic $BaCoO_{2.667}$ [56], in which d^5 configured Co^{4+} was also located on the tetrahedral site, and for which neutron diffraction data could be recorded. The magnetic moments derived from the Bader analysis (see Table S 2) are found to be smaller than expected from the nominal oxidation numbers. Such a quantitative deviation is found also for transition metal oxides like TiO_2 [77] and actually under active discussion [78]. It is nevertheless noteworthy that the Bader-derived magnetic moments of Fe well distinguish the tetrahedrally coordinated site from the pyramidal or the octahedral site, consistently with BVS (again see Table 4).

The allocation of Fe^{4+} on the tetrahedral site is further in agreement with the Mössbauer data, where the B_{hf} values and isomer shifts for octahedral / square pyramidal coordination of Fe^{3+} are similar to what was found in $BaFeO_{2.5}$ [20] and $BaFeO_{2.333}F_{0.333}$. Thus we conclude that, though Jahn–Teller stabilizing coordination geometries (octahedral / square pyramidal) are available in the structural setting of $BaFeO_{2.667}$, there is a size-driven tendency of Fe^{4+} to be located on the tetrahedrally coordinated site. However, a conclusion about the distortion of the tetrahedron cannot be drawn due to a lack of reliable positional parameters of the anions.

Table 4. Bond valence sums (BVS) [76] calculated for different cations. Magnetic moments on atoms derived from the Bader analysis (Table S 2) are also shown for comparison.

Atom	Distances to oxygen (Å)	BVS	M (μ_B)
Ba1	1x 2.676 2x 2.752 2x 2.763 1x 2.809 2x 2.877 2x 3.165	+2.32	
Ba2	1x 2.744 2x 2.836 2x 2.847 2x 2.949 2x 3.088 1x 3.165	+1.85	
Ba3	1x 2.812 2x 2.845 2x 2.851 2x 2.902 1x 2.946 2x 3.018 2x 3.186	+2.12	

Fe1 (pyramidal)	1x 1.916 2x 1.974 2x 2.047	+2.71	3.88
Fe2 (tetrahedral)	1x 1.742 1x 1.776 2x 1.852	+3.58	3.19
Fe3 (octahedral)	1x 1.971 2x 2.036 2x 2.038 1x 2.463	+2.61	3.94

Further, it is also appropriate to discuss the structure found for $BaFeO_{2.667}$ to earlier reported structural models for this compound. Though no diffraction data and details of powder preparation are presented in the early report from Mori in 1965 [79], we assume that the author might have prepared this phase (which was described as triclinic-II) before by heating $BaFeO_{2.5}$ (which was referred to as triclinic-I phase) between 400-500 °C in oxygen atmosphere. However, the lattice parameters reported (a ≈ b ≈ 405.0 pm, c ≈ 402.4 pm, α ≈ 91°44', β ≈ 88°16', γ ≈ 91°51') are implausible, since in such a small cell only compositions according to ABX_{3-n} (n = 0, 1, 2, or 3) will be possible; clearly, the obtained splitting pattern cannot well describe the splitting of the main reflections and also does not cause superstructure reflections. The fact that many perovskite related barium ferrates were originally discovered in the 1960s, but could be only structurally solved in the early 90s or even later by neutron or electron diffraction, points to the high structural complexity found for this class of materials, the difficulty of growing single crystals due to the topochemical nature of the oxygen uptake / release, and the difficulty to solve such structures based on powder diffraction datasets.

3.3 Magnetic characterization of $BaFeO_{2.667}$

Figure 6 a,b shows the magnetization of $BaFeO_{2.667}$ as a function of temperature and the magnetization as a function of external field, respectively. Since the powder used for magnetic characterization also contains a small amount of tetragonal $BaFeO_{2.81}$ (see previous sections), we also performed a magnetic characterization (see Figure S 2 in Electronic Supplementary Material). From the significantly different behavior, we conclude that the magnetic properties measured above 80 K most likely correspond to the monoclinic $BaFeO_{2.667}$ phase with $P2_1/m$ symmetry, since $BaFeO_{2.81}$ is paramagnetic with a very low overall magnetization above this temperature.

Above about 310 K, the magnetization curves of $BaFeO_{2.667}$ in Figure 6 a,b show a plateau which might be a result of small (anti)ferromagnetic domains. Furthermore, close to 350 K, the zero-field-cooled magnetization increases slightly with increasing temperature, which could

indicate an antiferromagnetic (possibly short-range) transition at higher temperatures. A Néel temperature above room temperature is also in agreement with the Mössbauer spectra recorded at room temperature (Figure S 1), which show the presence of a dynamic sextet along with singlet and two doublets next to it. This indicates on-going loss of long-range magnetic ordering. At around 300 K, the magnetization curves show a ferromagnetic-like transition, which is probably due to weak ferromagnetism on top of the dominant antiferromagnetic order, as the magnetization measurements (Figure 6 b) do not show any saturation or hysteresis at 250 K. Below the transition at around 300 K, the FC and ZFC curves diverge notably, confirming a weak ferromagnetic (or a spin-glass-like) behavior, which is common in oxygen defect materials with canted or locally uncompensated spins [80]. At about 55 K there is a maximum visible in the ZFC curve and to a lesser extent in the FC curve, which could be related either to gradual strengthening of the magnetic order with the decreasing temperature or presence of the magnetic coercivity. Indeed, at low temperatures, magnetic hysteresis was observed in the magnetization curves, with coercivity reaching about 700 Oe at 10 K, as shown in the inset in Figure 6 b. The M(H) curve measured below and above the transitions (Figure 6 b) showed linear behavior without saturation, which again indicates a prevailing antiferromagentic order with spin canting or locally uncompensated spins in the whole temperature range. However, we acknowledge that the behavior below 150 K cannot be assigned to $BaFeO_{2.667}$ with high certainity, due to a similar response of $BaFeO_{2.81}$ below 150 K, which might overlap with the magnetic feature of $BaFeO_{2.667}$.

Previous experiments for barium ferrates such as $BaFeO_{2.5}$ [20] or $BaFeO_{2.333}F_{0.333}$ [30], which are both oxygen-vacancy-ordered derivatives of the cubic perovskite aristotype structure, found the G-AFM ordering according to the Wollan–Koehler notation [81]. This magnetic ordering is in general favoured for iron-based perovskites, due to the fact that the Fe-O-Fe bond angle only slightly deviates from 180°, thus inducing strong antiferromagnetic superexchange interactions [82].

Attempts were made to confirm the principle stability of an antiferromagnetic configuration over ferromagnetic and nonmagnetic configurations by *ab initio* calculations for $BaFeO_{2.667}$. Indeed, G-type AFM ordering (see Figure 7 a) was found to be energetically most stable as compared to the FM and the NM configurations (see Figure 7 b) regardless the U_{eff} value, giving good agreement to the observed experimental findings. Our DFT results also show that the ordered oxygen vacancies in $Ba_3Fe_3O_8$ change the stable magnetic state as compared to $BaFeO_3$ (i.e., of the perfect cubic perovskite without oxygen vacancies), for which the FM ordering is energetically more stable than various other AFM orderings within collinear spin polarized calculations [51-53]. Further, for G-type AFM $Ba_3Fe_3O_8$, all magnetic moments on Fe are larger than

3 μ_B for all the sites, indicating again that the Fe cations are in high-spin states (see Table 4 and Table S 2).

Though the above made interpretation of the magnetic behavior observed experimentally is fully consistent with the DFT calculations and to what has been found previously on related iron-based perovskite, we acknowledge that further experiments, including temperature dependent neutron diffraction studies, would be required to achieve a final proof for the suggested magnetic behavior.

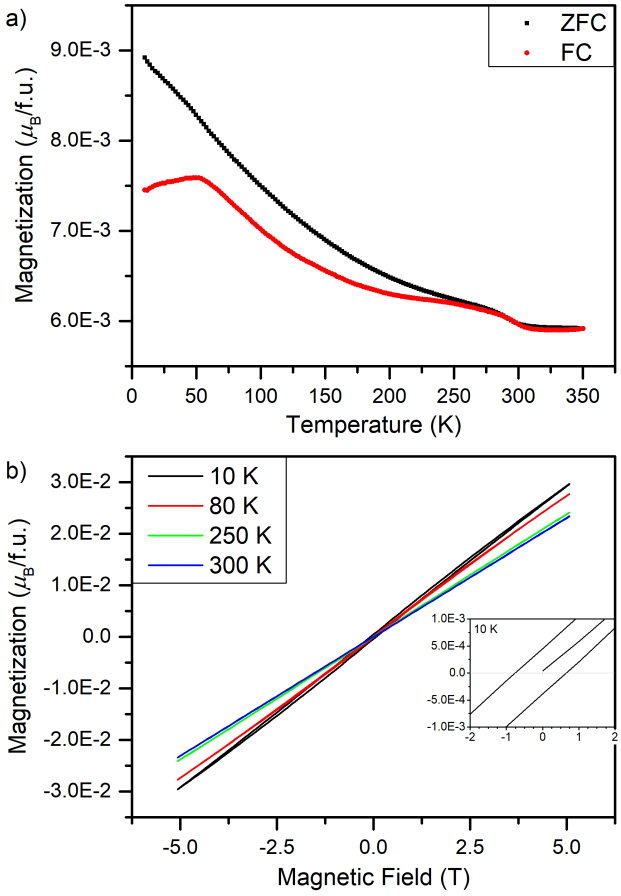

Figure 6. a) Field cooled and zero field cooled curves and b) Field-dependent magnetization of $BaFeO_{2.667}$ at various temperatures with the coercivity at 10 K shown in the inset.

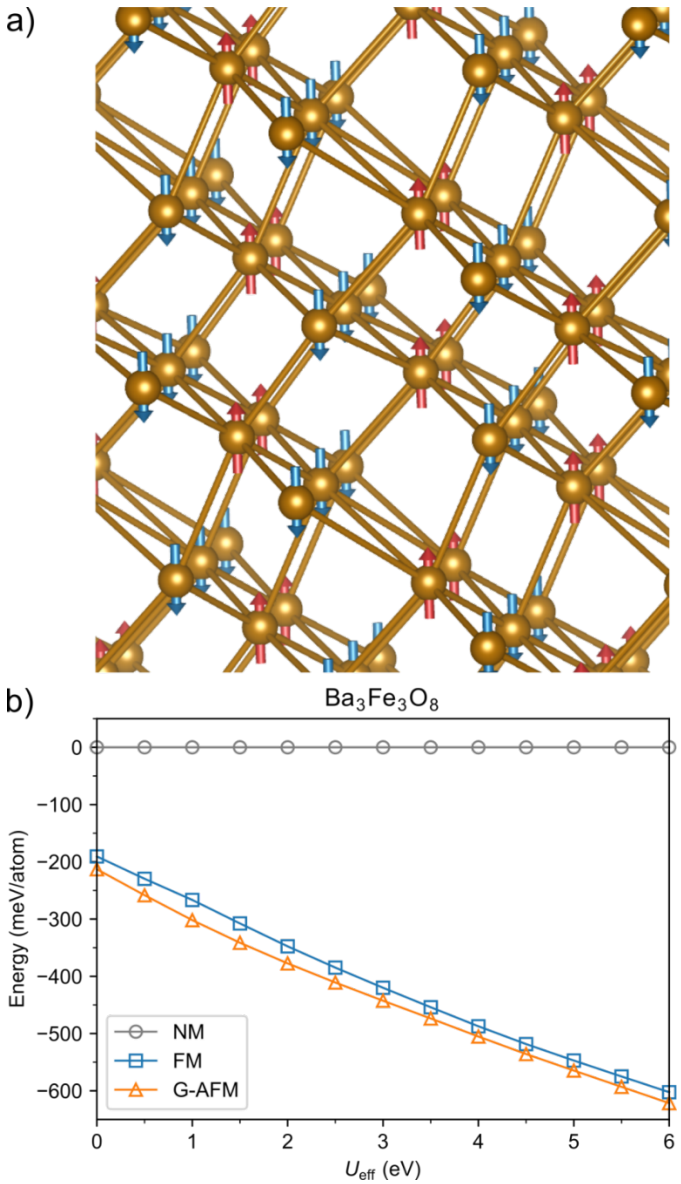

Figure 7. a) Energetically most stable G-type AFM ordering of $Ba_3Fe_3O_8$, with only the Fe atoms shown. The red and the blue arrows indicate spin-up and spin-down magnetic moments, respectively. For each Fe atom, its six neighboring Fe atoms have opposite magnetic moments; b) a*b initio* computed energies of $Ba_3Fe_3O_8$ as a function of U_{eff}. For each U_{eff}, the energy of the NM phase is set as the reference.

4 Conclusions

In this study, we have presented a detailed analysis of the structural, electric and magnetic properties of charge-ordered $BaFeO_{2.667}$, which reveals itself to be isotypic to $BaFeO_{2.333}F_{0.333}$. XRD experiments together with *ab initio* calculations confirm the structural model based on the space group $P2_1/m$. Mössbauer spectroscopy indicates three differently coordinated iron sites with Fe^{3+} being coordinated inside an octahedron and in a square pyramid, while Fe^{4+} is found to be coordinated inside of a tetrahedron. Magnetic measurements suggest an antiferromagnetic behavior, and *ab initio* GGA+*U* simulations also support the G-AFM ordering of $Ba_3Fe_3O_8$, and

the Bader-analysis-obtained atomic magnetic moments on Fe as well as bond valence sums can be interpreted consistently with the expected oxidation numbers from the Mössbauer spectroscopy. Based on these results we can state, to the best of our knowledge, that $BaFeO_{2.667}$ exhibits the only tetrahedrally coordinated Fe^{4+} cation inside a vacancy ordered perovskite lattice which is derived from the cubic aristotype structure.

The performed HT-XRD and TG/DTA experiments reveal the complex oxidation and reduction of the mother compound $BaFeO_{2.5}$ and suggest a lattice enthalpy driven structural transition. On the other side, the high temperature cubic configuration is shown to preserve the oxygen stoichiometry while undergoing the strongly endothermic phase transition from the oxygen vacancy ordered $P2_1/c$ structure. In addition, the formation and stability of the presented oxidized phase seems to be strongly depending of the oxygen partial pressure as suggested by comparative HT-XRD experiments under air.

Further, we found that changes of the synthesis procedure, can also alternate the oxygen uptake and release behavior of $BaFeO_{2.667}$, which alters the electrical properties of the material significantly, and we aim to address this finding in more detail in a follow-up study.

5 Acknowledgments

S.W. and O.C. acknowledge funding by the German Research Foundation (DFG) within CL551/2-1. Y.I. and B.G. acknowledge support by the state of Baden-Württemberg through bwHPC and the German Research Foundation (DFG) through grant no. INST 40/575-1 FUGG (JUSTUS 2 cluster) and funding from the European Research Council (ERC) under the European Union's Horizon 2020 research and innovation programme (grant agreement no. 865855).

6 Supporting Information

Room temperature ^{57}Fe Mössbauer spectrum and fit, Nyquist and Bode plots and fits of cyclic high temperature impedance spectroscopy, XRD patterns of symmetrical films prior and after to impedance spectroscopy, comments on Bader analysis, detailed interpretation of TG/DTA measurement.

7 References

1. Skinner, S. J. Recent advances in Perovskite-type materials for solid oxide fuel cell cathodes. *International Journal of Inorganic Materials* **2001,** 3 (2), 113-121 DOI: 10.1016/s1466-6049(01)00004-6.

2. Richter, J.; Holtappels, P.; Graule, T.; Nakamura, T.; Gauckler, L. J. Materials design for perovskite SOFC cathodes. *Monatshefte für Chemie - Chemical Monthly* **2009,** 140 (9), 985-999 DOI: 10.1007/s00706-009-0153-3.

3. Sun, C.; Hui, R.; Roller, J. Cathode materials for solid oxide fuel cells: a review. *Journal of Solid State Electrochemistry* **2009,** 14 (7), 1125-1144 DOI: 10.1007/s10008-009-0932-0.

4. Zhou, W.; Ran, R.; Shao, Z. Progress in understanding and development of $Ba_{0.5}Sr_{0.5}Co_{0.8}Fe_{0.2}O_{3-\delta}$-based cathodes for intermediate-temperature solid-oxide fuel cells: A review. *Journal of Power Sources* **2009,** 192 (2), 231-246 DOI: 10.1016/j.jpowsour.2009.02.069.

5. Mastrikov, Y. A.; Kuklja, M. M.; Kotomin, E. A.; Maier, J. First-principles modelling of complex perovskite $(Ba_{1-x}Sr_x)(Co_{1-y}Fe_y)O_{3-\delta}$ for solid oxide fuel cell and gas separation membrane applications. *Energy & Environmental Science* **2010,** 3 (10), DOI: 10.1039/c0ee00096e.

6. Tong, J. Investigation of ideal zirconium-doped perovskite-type ceramic membrane materials for oxygen separation. *Journal of Membrane Science* **2002,** 203 (1-2), 175-189 DOI: 10.1016/s0376-7388(02)00005-4.

7. Vieten, J.; Bulfin, B.; Call, F.; Lange, M.; Schmücker, M.; Francke, A.; Roeb, M.; Sattler, C. Perovskite oxides for application in thermochemical air separation and oxygen storage. *Journal of Materials Chemistry A* **2016,** 4 (35), 13652-13659 DOI: 10.1039/c6ta04867f.

8. Mats, J.; Lemmens, P. In *Handbook of Magnetism and Advanced Magnetic Materials*; John Wiley & Sons, Ltd: 2007.

9. Zhang, Z.; Zhu, Y.; Zhong, Y.; Zhou, W.; Shao, Z. Anion Doping: A New Strategy for Developing High-Performance Perovskite-Type Cathode Materials of Solid Oxide Fuel Cells. *Advanced Energy Materials* **2017,** 7 (17), DOI: 10.1002/aenm.201700242.

10. Zhu, J.; Liu, G.; Liu, Z.; Chu, Z.; Jin, W.; Xu, N. Unprecedented Perovskite Oxyfluoride Membranes with High-Efficiency Oxygen Ion Transport Paths for Low-Temperature Oxygen Permeation. *Adv Mater* **2016,** 28 (18), 3511-5 DOI: 10.1002/adma.201505959.

11. Dai, H. X.; Ng, C. F.; Au, C. T. The catalytic performance and characterization of a durable perovskite-type chloro-oxide $SrFeO_{3-\delta}Cl_{\sigma}$ catalyst selective for the oxidative dehydrogenation of ethane. *Catalysis Letters* **1999,** 57 (3), 115-120 DOI: 10.1023/a:1019091414588.

12. Dai, H. X.; Ng, C. F.; Au, C. T. Perovskite-Type Halo-oxide $La_{1-x}Sr_xFeO_{3-\delta}X_\sigma$ (X=F, Cl) Catalysts Selective for the Oxidation of Ethane to Ethene. *Journal of Catalysis* **2000,** 189 (1), 52-62 DOI: 10.1006/jcat.1999.2677.

13. Yin, W.-J.; Yang, J.-H.; Kang, J.; Yan, Y.; Wei, S.-H. Halide perovskite materials for solar cells: a theoretical review. *Journal of Materials Chemistry A* **2015,** 3 (17), 8926-8942 DOI: 10.1039/c4ta05033a.

14. Colville, A. A.; Geller, S. The crystal structure of brownmillerite, Ca_2FeAlO_5. *Acta Crystallographica Section B Structural Crystallography and Crystal Chemistry* **1971,** 27 (12), 2311-2315 DOI: 10.1107/s056774087100579x.

15. Shin, S.; Yonemura, M.; Ikawa, H. Order-disorder transition of $Sr_2Fe_2O_5$ from brownmillerite to perovskite structure at an elevated temperature. *Materials Research Bulletin* **1978,** 13 (10), 1017-1021 DOI: 10.1016/0025-5408(78)90166-6.

16. Gallagher, P. K.; MacChesney, J. B.; Buchanan, D. N. E. Mössbauer Effect in the System $BaFeO_{2.5-3.0}$. *The Journal of Chemical Physics* **1965,** 43 (2), 516-520 DOI: 10.1063/1.1696774.

17. MacChesney, J. B.; Sherwood, R. C.; Potter, J. F. Electric and Magnetic Properties of the Strontium Ferrates. *The Journal of Chemical Physics* **1965,** 43 (6), 1907-1913 DOI: 10.1063/1.1697052.

18. Köhler, J. Square-planar coordinated iron in the layered oxoferrate(II) $SrFeO_2$. *Angew Chem Int Ed Engl* **2008,** 47 (24), 4470-2 DOI: 10.1002/anie.200800855.

19. Yamamoto, T.; Kobayashi, Y.; Hayashi, N.; Tassel, C. d.; Saito, T.; Yamanaka, S.; Takano, M.; Ohoyama, K.; Shimakawa, Y.; Yoshimura, K. $(Sr_{1-x}Ba_x)FeO_2$ ($0.4 \leq x \leq 1$): A New Oxygen-Deficient Perovskite Structure. *Journal of the American Chemical Society* **2012,** 134 (28), 11444-11454.

20. Clemens, O.; Groting, M.; Witte, R.; Perez-Mato, J. M.; Loho, C.; Berry, F. J.; Kruk, R.; Knight, K. S.; Wright, A. J.; Hahn, H.; Slater, P. R. Crystallographic and magnetic structure of the perovskite-type compound $BaFeO_{2.5}$: unrivaled complexity in oxygen vacancy ordering. *Inorg Chem* **2014,** 53 (12), 5911-21 DOI: 10.1021/ic402988y.

21. Parras, M.; Fournes, L.; Grenier, J. C.; Pouchard, M.; Vallet, M.; Calbet, J. M.; Hagenmuller, P. Structural aspects and Mössbauer resonance investigation of $Ba_2Fe_2O_5$. *Journal of Solid State Chemistry* **1990,** 88 (1), 261-268 DOI: 10.1016/0022-4596(90)90223-k.

22. Parras, M.; Vallet-Regi, M.; Gonzalez-Calbet, J. M.; Alario-Franco, M. A.; Grenier, J. C.; Hagenmuller, P. A reassessment of $Ba_2Fe_2O_5$. *Materials Research Bulletin* **1987,** 22 (10), 1413-1419 DOI: 10.1016/0025-5408(87)90306-0.

23. Mori, S. Phase Transformation in Barium Orthoferrate, $BaFeO_{3-x}$. *Journal of the American Ceramic Society* **1966,** 49 (11), 600-605 DOI: 10.1111/j.1151-2916.1966.tb13176.x.

24. Suga, Y.; Hibino, M.; Kudo, T.; Mizuno, N. Electrochemical Oxidation of $BaFeO_{2.5}$ to $BaFeO_3$. *Electrochimica Acta* **2014,** 137, 359-362 DOI: 10.1016/j.electacta.2014.05.162.

25. Lucchini, E.; Meriani, S.; Minichelli, D. An X-ray study of two phases of $BaFeO_{3-x}$. *Acta Crystallographica Section B Structural Crystallography and Crystal Chemistry* **1973,** 29 (6), 1217-1219 DOI: 10.1107/s0567740873004255.

26. Gómez, M. I.; Lucotti, G.; de Morán, J. A.; Aymonino, P. J.; Pagola, S.; Stephens, P.; Carbonio, R. E. Ab Initio Structure Solution of $BaFeO_{2.8-\delta}$, a New Polytype in the System $BaFeO_y$ ($2.5 \leq y \leq 3.0$) Prepared from the Oxidative Thermal Decomposition of $BaFe[(CN)_5NO]\cdot 3H_2O$. *Journal of Solid State Chemistry* **2001,** 160 (1), 17-24 DOI: 10.1006/jssc.2001.9119.

27. Goldschmidt, V. M. Die Gesetze der Krystallochemie. *Die Naturwissenschaften* **1926,** 14 (21), 477-485 DOI: 10.1007/bf01507527.

28. Heap, R.; Slater, P. R.; Berry, F. J.; Helgason, O.; Wright, A. J. Synthesis and structural determination of the new oxide fluoride $BaFeO_2F$. *Solid State Communications* **2007,** 141 (8), 467-470 DOI: 10.1016/j.ssc.2006.11.037.

29. Clemens, O. Structural characterization of a new vacancy ordered perovskite modification found for $Ba_3Fe_3O_7F$ ($BaFeO_{2.333}F_{0.333}$): Towards understanding of vacancy ordering for different perovskite-type ferrites. *Journal of Solid State Chemistry* **2015,** 225, 261-270 DOI: 10.1016/j.jssc.2014.12.027.

30. Clemens, O.; Reitz, C.; Witte, R.; Kruk, R.; Smith, R. I. Anion ordering, magnetic structure and properties of the vacancy ordered perovskite $Ba_3Fe_3O_7F$. *Journal of Solid State Chemistry* **2016,** 243, 31-37 DOI: 10.1016/j.jssc.2016.07.033.

31. Benes, A.; Molinari, A.; Witte, R.; Kruk, R.; Brotz, J.; Chellali, R.; Hahn, H.; Clemens, O. Proton Conduction in Grain-Boundary-Free Oxygen-Deficient $BaFeO_{2.5+\delta}$ Thin Films. *Materials (Basel)* **2017,** 11 (1), DOI: 10.3390/ma11010052.

32. Knöchel, P. L.; Keenan, P. J.; Loho, C.; Reitz, C.; Witte, R.; Knight, K. S.; Wright, A. J.; Hahn, H.; Slater, P. R.; Clemens, O. Synthesis, structural characterisation and proton conduction of two new hydrated phases of barium ferrite $BaFeO_{2.5-x}(OH)_{2x}$. *J. Mater. Chem. A* **2016,** 4 (9), 3415-3430 DOI: 10.1039/c5ta06383c.

33. Hayashi, N.; Yamamoto, T.; Kageyama, H.; Nishi, M.; Watanabe, Y.; Kawakami, T.; Matsushita, Y.; Fujimori, A.; Takano, M. $BaFeO_3$: a ferromagnetic iron oxide. *Angew Chem Int Ed Engl* **2011,** 50 (52), 12547-50 DOI: 10.1002/anie.201105276.

34. Rahman, G.; Sarwar, S. Ground State Structure of $BaFeO_3$: Density Functional Theory Calculations. *Journal of Superconductivity and Novel Magnetism* **2017,** 31 (2), 413-418 DOI: 10.1007/s10948-017-4223-1.

35. Wollstadt, S.; Clemens, O. On the Impact of the Degree of Fluorination on the ORR Limiting Processes within Iron Based Catalysts: A Model Study on Symmetrical Films of Barium Ferrate. *Materials (Basel)* **2020,** 13 (11), DOI: 10.3390/ma13112532.

36. Niu, Y.; Zhou, W.; Sunarso, J.; Liang, F.; Zhu, Z.; Shao, Z. A single-step synthesized cobalt-free barium ferrites-based composite cathode for intermediate temperature solid oxide fuel cells. *Electrochemistry Communications* **2011,** 13 (12), 1340-1343 DOI: 10.1016/j.elecom.2011.08.007.

37. Masunaga, T.; Izumi, J.; Miura, N. Reversible change in crystal structure of Ba(or Sr)$FeO_{3-\delta}$ associated with oxygen sorption/desorption by pressure variation. *Journal of the Ceramic Society of Japan* **2010,** 118 (1382), 952-954 DOI: 10.2109/jcersj2.118.952.

38. Benel, C.; Darbandi, A. J.; Djenadic, R.; Evans, A.; Tölke, R.; Prestat, M.; Hahn, H. Synthesis and characterization of nanoparticulate $La_{0.6}Sr_{0.4}CoO_{3-\delta}$ cathodes for thin-film solid oxide fuel cells. *Journal of Power Sources* **2013,** 229, 258-264 DOI: 10.1016/j.jpowsour.2012.11.149.

39. Djenadic, R.; Botros, M.; Benel, C.; Clemens, O.; Indris, S.; Choudhary, A.; Bergfeldt, T.; Hahn, H. Nebulized spray pyrolysis of Al-doped $Li_7La_3Zr_2O_{12}$ solid electrolyte for battery applications. *Solid State Ionics* **2014,** 263, 49-56 DOI: 10.1016/j.ssi.2014.05.007.

40. Blochl, P. E. Projector augmented-wave method. *Phys Rev B Condens Matter* **1994,** 50 (24), 17953-17979 DOI: 10.1103/physrevb.50.17953.

41. Kresse, G.; Furthmuller, J. Efficient iterative schemes for ab initio total-energy calculations using a plane-wave basis set. *Phys Rev B Condens Matter* **1996,** 54 (16), 11169-11186 DOI: 10.1103/physrevb.54.11169.

42. Kresse, G.; Furthmüller, J. Efficiency of ab-initio total energy calculations for metals and semiconductors using a plane-wave basis set. *Computational Materials Science* **1996,** 6 (1), 15-50 DOI: 10.1016/0927-0256(96)00008-0.

43. Kresse, G.; Joubert, D. From ultrasoft pseudopotentials to the projector augmented-wave method. *Physical Review B* **1999,** 59 (3), 1758-1775 DOI: 10.1103/PhysRevB.59.1758.

44. Methfessel, M.; Paxton, A. T. High-precision sampling for Brillouin-zone integration in metals. *Phys Rev B Condens Matter* **1989,** 40 (6), 3616-3621 DOI: 10.1103/physrevb.40.3616.

45. Dudarev, S. L.; Botton, G. A.; Savrasov, S. Y.; Humphreys, C. J.; Sutton, A. P. Electron-energy-loss spectra and the structural stability of nickel oxide: An LSDA+U study. *Physical Review B* **1998,** 57 (3), 1505-1509 DOI: 10.1103/PhysRevB.57.1505.

46. Bader, R. F. W. *Atoms in Molecules. A Quantum Theory. (International Series of Monographs on Chemistry, Vol. 22.)*. 1992; Vol. 104, p 1423-1423.

47. Yu, M.; Trinkle, D. R. Accurate and efficient algorithm for Bader charge integration. *J Chem Phys* **2011,** 134 (6), 064111 DOI: 10.1063/1.3553716.

48. Henkelman, G.; Arnaldsson, A.; Jónsson, H. A fast and robust algorithm for Bader decomposition of charge density. *Computational Materials Science* **2006,** 36 (3), 354-360 DOI: 10.1016/j.commatsci.2005.04.010.

49. Sanville, E.; Kenny, S. D.; Smith, R.; Henkelman, G. Improved grid-based algorithm for Bader charge allocation. *J Comput Chem* **2007,** 28 (5), 899-908 DOI: 10.1002/jcc.20575.

50. Tang, W.; Sanville, E.; Henkelman, G. A grid-based Bader analysis algorithm without lattice bias. *J Phys Condens Matter* **2009,** 21 (8), 084204 DOI: 10.1088/0953-8984/21/8/084204.

51. Ribeiro, B.; Godinho, M.; Cardoso, C.; Borges, R. P.; Gasche, T. P. Self-doping and the role of oxygen vacancies in the magnetic properties of cubic $BaFeO_{3-\delta}$. *Journal of Applied Physics* **2013,** 113 (8), DOI: 10.1063/1.4792664.

52. Cherair, I.; Iles, N.; Rabahi, L.; Kellou, A. Effects of Fe substitution by Nb on physical properties of $BaFeO_3$: A DFT+*U* study. *Computational Materials Science* **2017,** 126, 491-502 DOI: 10.1016/j.commatsci.2016.10.018.

53. Cherair, I.; Bousquet, E.; Schmitt, M. M.; Iles, N.; Kellou, A. First-principles study of strain-induced Jahn-Teller distortions in $BaFeO_3$. *J Phys Condens Matter* **2018,** 30 (25), 255701 DOI: 10.1088/1361-648X/aac46d.

54. Clevenger, T. R. Effect of Fe^{4+} in the System $SrFeO_3$-$SrTiO_3$. *Journal of the American Ceramic Society* **1963,** 46 (5), 207-210 DOI: 10.1111/j.1151-2916.1963.tb19773.x.

55. Nassau, K. A model for the Fe^{2+}-Fe^{4+} equilibrium in flux-grown yttrium iron garnet. *Journal of Crystal Growth* **1968,** 2 (4), 215-221 DOI: 10.1016/0022-0248(68)90004-3.

56. Waidha, A. I.; Siddiqi, H. K.; Ikeda, Y.; Lepple, M.; Vasala, S.; Donzelli, M.; Fortes, A. D.; Slater, P.; Grabowski, B.; Kramm, U. I.; Clemens, O. Structural, Magnetic and Catalytic Properties of a New Vacancy Ordered Perovskite Type Barium Cobaltate BaCoO2.67. *Chemistry* **2021**, DOI: 10.1002/chem.202101167.

57. Wollstadt, S.; De Souza, R. A.; Clemens, O. Kinetic Study of the Interdiffusion of Fluorine and Oxygen in the Perovskite-Type Barium Ferrate System $BaFeO_{2.5-x}F_{2x}$. *The Journal of Physical Chemistry C* **2021**, DOI: 10.1021/acs.jpcc.0c10174.

58. Li, Z.; Laskowski, R.; Iitaka, T.; Tohyama, T. First-principles calculation of helical spin order in iron perovskite $SrFeO_3$ and $BaFeO_3$. *Physical Review B* **2012,** 85 (13), DOI: 10.1103/PhysRevB.85.134419.

59. Jeannot, C.; Malaman, B.; Gérardin, R.; Oulladiaf, B. Synthesis, Crystal and Magnetic Structures of the Sodium Ferrate (IV) Na_4FeO_4 Studied by Neutron Diffraction and Mössbauer Techniques. *Journal of Solid State Chemistry* **2002,** 165 (2), 266-277 DOI: 10.1006/jssc.2002.9520.

60. Delattre, J. L.; Stacy, A. M.; Young, V. G., Jr.; Long, G. J.; Hermann, R.; Grandjean, F. Study of the structural, electronic, and magnetic properties of the barium-rich iron(IV) oxides, Ba_2FeO_4 and Ba_3FeO_5. *Inorg Chem* **2002,** 41 (11), 2834-8 DOI: 10.1021/ic0113247.

61. Takano, M.; Takeda, Y. Electronic State of Fe^{4+} Ions in Perovskite-Type Oxides. **1983**.

62. Hosaka, Y.; Ichikawa, N.; Saito, T.; Manuel, P.; Khalyavin, D.; Attfield, J. P.; Shimakawa, Y. Two-dimensional charge disproportionation of the unusual high valence state Fe^{4+} in a layered double perovskite. *J Am Chem Soc* **2015,** 137 (23), 7468-73 DOI: 10.1021/jacs.5b03712.

63. Bocquet, A. E.; Fujimori, A.; Mizokawa, T.; Saitoh, T.; Namatame, H.; Suga, S.; Kimizuka, N.; Takeda, Y.; Takano, M. Electronic structure of $SrFe^{4+}O_3$ and related Fe perovskite oxides. *Phys Rev B Condens Matter* **1992,** 45 (4), 1561-1570 DOI: 10.1103/physrevb.45.1561.

64. Vračar, M.; Kuzmin, A.; Merkle, R.; Purans, J.; Kotomin, E. A.; Maier, J.; Mathon, O. Jahn-Teller distortion around Fe^{4+} in $Sr(Fe_xTi_{1-x})O_{3-\delta}$ from x-ray absorption spectroscopy, x-ray diffraction, and vibrational spectroscopy. *Physical Review B* **2007,** 76 (17), DOI: 10.1103/PhysRevB.76.174107.

65. Luo, K.; Johnson, R. D.; Tran, T. T.; Halasyamani, P. S.; Radaelli, P. G.; Hayward, M. A. $Ba_2YFeO_{5.5}$: A Ferromagnetic Pyroelectric Phase Prepared by Topochemical Oxidation. *Chemistry of Materials* **2013,** 25 (9), 1800-1808 DOI: 10.1021/cm400364y.

66. Hodges, J. P.; Short, S.; Jorgensen, J. D.; Xiong, X.; Dabrowski, B.; Mini, S. M.; Kimball, C. W. Evolution of Oxygen-Vacancy Ordered Crystal Structures in the Perovskite Series $Sr_nFe_nO_{3n-1}$ (n=2, 4, 8, and ∞), and the Relationship to Electronic and Magnetic Properties. *Journal of Solid State Chemistry* **2000,** 151 (2), 190-209 DOI: 10.1006/jssc.1999.8640.

67. Waerenborgh, J. C.; Rojas, D. P.; Vyshatko, N. P.; Shaula, A. L.; Kharton, V. V.; Marozau, I. P.; Naumovich, E. N. Fe^{4+} formation in brownmillerite $CaAl_{0.5}Fe_{0.5}O_{2.5+\delta}$. *Materials Letters* **2003,** 57 (28), 4388-4393 DOI: 10.1016/s0167-577x(03)00330-6.

68. Bland, J. A. The crystal structure of barium orthotitanate, Ba_2TiO_4. *Acta Crystallographica* **1961,** 14 (8), 875-881 DOI: 10.1107/s0365110x61002527.

69. Chamberland, B. L.; Herrero-Fernandez, M. P.; Hewston, T. A. Magnetic behavior of tetrahedral Cr^{4+} compounds: Sr_2CrO_4, Ba_2CrO_4, and Ba_3CrO_5. *Journal of Solid State Chemistry* **1985,** 59 (1), 111-115 DOI: 10.1016/0022-4596(85)90357-3.

70. Dann, S. E.; Weller, M. T.; Currie, D. B. The synthesis and structure of Sr_2FeO_4. *Journal of Solid State Chemistry* **1991,** 92 (1), 237-240 DOI: 10.1016/0022-4596(91)90263-h.

71. Mattausch, H.; Müller-Buschbaum, H. Zur Kenntnis von Ba_2CoO_4. *Zeitschrift für anorganische und allgemeine Chemie* **1971,** 386 (1), 1-14 DOI: 10.1002/zaac.19713860102.

72. Mattausch, H.; Müller-Buschbaum, H. Zur Kristallstruktur von Ba_2CrO_4. *Zeitschrift fr anorganische und allgemeine Chemie* **1974,** 407 (2), 129-134 DOI: 10.1002/zaac.19744070202.

73. Feltz, A.; Schmalfuß, S. Untersuchungen an elektronenleitenden Oxidsystemen; Zur Darstellung der Verbindungen Ba_2VO_4 und Sr_2VO_4 und die Reduktion von $Ca_2V_2O_7$ im H_2-Strom. *Zeitschrift für Chemie* **1975,** 15 (7), 289-291 DOI: 10.1002/zfch.19750150722.

74. Liu, G.; Greedan, J. E. Synthesis and Characterization of Ba_2VO_4 with the β-Ca_2SiO_4 Structure: Comparison with Sr_2VO_4. *Journal of Solid State Chemistry* **1993,** 103 (1), 228-239 DOI: 10.1006/jssc.1993.1095.

75. Gütlich, P.; Bill, E.; Trautwein, A. X. *Mössbauer Spectroscopy and Transition Metal Chemistry*. 2011.

76. Brown, I. D.; Altermatt, D. Bond-valence parameters obtained from a systematic analysis of the Inorganic Crystal Structure Database. *Acta Crystallographica Section B Structural Science* **1985,** 41 (4), 244-247 DOI: 10.1107/s0108768185002063.

77. Koch, D.; Manzhos, S. On the charge state of titanium in titanium dioxide. *The journal of physical chemistry letters* **2017,** 8 (7), 1593-1598.

78. Walsh, A.; Sokol, A. A.; Buckeridge, J.; Scanlon, D. O.; Catlow, C. R. A. Oxidation states and ionicity. *Nature materials* **2018,** 17 (11), 958-964.

79. Mori, S. Preparation of Various Phases of $BaFeO_{3-x}$. *Journal of the American Ceramic Society* **1965,** 48 (3), 165-165 DOI: 10.1111/j.1151-2916.1965.tb16058.x.

80. Nair, A.; Wollstadt, S.; Witte, R.; Dasgupta, S.; Kehne, P.; Alff, L.; Komissinskiy, P.; Clemens, O. Synthesis and characterisation of fluorinated epitaxial films of $BaFeO_2F$: tailoring magnetic anisotropy via a lowering of tetragonal distortion. *RSC Advances* **2019,** 9 (64), 37136-37143 DOI: 10.1039/c9ra08039b.

81. Wollan, E. O.; Koehler, W. C. Neutron Diffraction Study of the Magnetic Properties of the Series of Perovskite-Type Compounds[(1−x)La, xCa]MnO_3. *Physical Review* **1955,** 100 (2), 545-563 DOI: 10.1103/PhysRev.100.545.

82. Clemens, O.; Marco, J. F.; Thomas, M. F.; Forder, S. D.; Zhang, H.; Cartenet, S.; Monze, A.; Bingham, P. A.; Slater, P. R.; Berry, F. J. Magnetic interactions in cubic-, hexagonal- and trigonal-barium iron oxide fluoride, $BaFeO_2F$. *J Phys Condens Matter* **2016,** 28 (34), 346001 DOI: 10.1088/0953-8984/28/34/346001.